RESEARCH ARTICLE
SPACE PHYSICS: MAGNETOSPHERIC PHYSICS

Earth and Planetary Physics
5: 32–41, 2021
doi: 10.26464/epp2021008

Formation of the mass density peak at the magnetospheric equator triggered by EMIC waves

ZuXiang Xue, ZhiGang Yuan*, XiongDong Yu, ShiYong Huang, and Zheng Qiao

School of Electronic Information, Wuhan University, Wuhan 420072, China

Key Points:

- Simultaneous observations of toroidal Alfvén and electromagnetic ion cyclotron waves determine distributions of the field line mass density.
- The heating of cold ions by EMIC waves can lead to the formation of the equatorial mass density peak.
- The paper provides an evidence that equatorial mass density peaks are formed due to equatorial ion concentrations triggered by EMIC waves.

Citation: Xue, Z. X., Yuan, Z. G., Yu, X. D., Huang, S. Y. and Qiao, Z. (2021). Formation of the mass density peak at the magnetospheric equator triggered by EMIC waves. *Earth Planet. Phys.*, *5*(1), 32–41. http://doi.org/10.26464/epp2021008

Abstract: We report a simultaneous observation of two band electromagnetic ion cyclotron (EMIC) waves and toroidal Alfvén waves by the Van Allen Probe mission. Through wave frequency analyses, the mass density ρ is found to be locally peaked at the magnetic equator. Perpendicular fluxes of ions (< 100 eV) increase simultaneously with the appearances of EMIC waves, indicating a heating of these ions by EMIC waves. In addition, the measured ion distributions also support the equatorial peak formation, which accords with the result of the frequency analyses. The formation of local mass density peaks at the equator should be due to enhancements of equatorial ion concentrations, which are triggered by EMIC waves' perpendicular heating on low energy ions.

Keywords: toroidal Alfvén waves; EMIC waves; magnetoseismology; equatorial mass density peak

1. Introduction

Mass density controls the time rate of the change of magnetohydrodynamic (MHD) processes and is important for the space weather. It plays a pivotal role in the dynamic evolution of heavy ion composition in the magnetosphere, which can significantly alter the properties of plasma waves (Rauch and Roux, 1982; Meredith et al., 2003; Shi QQ et al., 2013; Min et al., 2015; Zong Q-G et al., 2017, Huang et al., 2020). The magnetospheric mass density is dependent on the number density and the ion components.

However, it is difficult to directly measure ion components because the dominant populations contributing to the mass density often have low temperature, and the spacecraft's potential prevents the low-energy ions from reaching onboard detectors (Denton, 2006; André and Cully, 2012). In order to determine the ion components and the mass density, many researchers resort to characteristic frequencies of plasma waves, e.g. electromagnetic ion cyclotron waves (Min et al., 2015; Kim et al., 2015) and toroidal Alfvén waves (Singer et al., 1981; Schulz, 1996; Denton et al., 2004, 2006, 2015; Denton, 2006; Takahashi et al., 2006, 2011; Takahashi and Denton, 2007; Min et al., 2013; Nosé et al., 2015).

Correspondence to: Z. G. Yuan, y_zgang@vip.163.com
Received 03 SEP 2020; Accepted 27 OCT 2020.
Accepted article online 25 DEC 2020.

Variations of mass density ρ along the magnetic field lines are often modeled by a power law function:

$$\rho = \rho_{eq}\left(\frac{LR_E}{R}\right)^{\alpha}, \quad (1)$$

where ρ_{eq} denotes the mass density at the magnetic equator, α decides the trend of ρ along the field line, and R_E, R, and L denote the Earth radius, the geocentric radius, and the L shell value (in units of R_E), respectively. For a positive (negative) α, ρ will increase (decrease) toward higher latitudes, while for $\alpha = 0$, ρ will be constant along the field line.

Previous researches have found $\alpha = 3$ in the plasmasphere for a diffusive equilibrium model (Angerami and Thomas, 1964) and $\alpha = 4$ in the plasmatrough for a collisionless model (Eviatar et al., 1964). Nosé et al. (2015) chose $\alpha = 0.5$ to study the formation process of an oxygen torus in the inner magnetosphere at $L = 3.0$–4.0 and $L = 3.7$–4.5. Denton et al. (2006) found $\alpha = 2$ appropriate for $L = 4$–5 and $\alpha = 1$ appropriate for $L = 5$–6 through studying the average values of toroidal Alfvén frequencies. Min et al. (2013) chose $\alpha = 1$ to derive the global equatorial mass density distribution covering radial distances from 4 to $9R_E$.

Nevertheless, observations also indicate the existence of $\alpha < 0$, which means a local peak of ρ at the magnetic equator. Takahashi and Denton (2007) found that there was evidence for $\alpha < 0$ in the afternoon magnetic local time (MLT) sector through statistically

studying the toroidal Alfvén frequencies measured by the Geostationary Operational Environmental Satellites (GOES) at geostationary orbit. Denton et al. (2004) also found a negative α for the power law mass density model through investigating toroidal Alfvén waves observed at MLT ~ 16.6 hr and $R \sim 6.4R_E$.

One possible reason for the peak of ρ_{eq} is that the centrifugal force acts more effectively on the heavier ions and preferentially traps them at the magnetic equator (Lemaire and Gringauz, 1998; Denton et al., 2006). Denton et al. (2015) demonstrated that the more negative α at dusk potentially arises from the greater contribution of trapped ring current particles (with tens of keV temperature), especially O^+, that drift westward from the magnetotail. In addition, perpendicular heating of cold ions by ion cyclotron waves may contribute to the formation of the local ρ_{eq} peak (Takahashi and Denton, 2007). However, direct observational evidence has not corroborated the formation of equatorial mass density peaks from perpendicular heating of cold ions by ion cyclotron waves.

In this paper, we present a typical case where toroidal Alfvén waves and two band EMIC waves are simultaneously observed. Wave frequency analyses illustrate that mass densities are locally enhanced at the equator. Through investigating measured ion fluxes, the formation of the mass density peak is shown to be promoted by the equatorial trapped ions, which are heated by EMIC waves.

2. Methods

2.1 Mass Density Derived from Toroidal Alfvén Waves

For the toroidal Alfvén mode waves in an arbitrary field model, the wave equation derived by Singer et al. (1981) is:

$$\frac{\partial^2}{\partial s^2}\left(\frac{\xi}{h}\right)+\frac{\partial}{\partial s}\ln\left(h^2B_0\right)\frac{\partial}{\partial s}\left(\frac{\xi}{h}\right)+\frac{\omega^2}{V_A^2}\left(\frac{\xi}{h}\right)=0, \tag{2}$$

where ξ is the field displacement in the azimuthal direction, and h is the scale factor for the normal separation between the field lines in the direction of oscillation which equals to $L\cos^3\lambda$ in the dipole field, where λ is the magnetic latitude. s is the distance along the field line with two ends fixed at ionosphere altitude (100 km in this work), ω is the frequency of toroidal mode waves, B_0 is the unperturbed magnetic field, and V_A is the Alfvén velocity equal to $B_0(\mu_0\rho)^{-1/2}$, where μ_0 is the free space permeability. With a shooting method (Press et al., 1997), Equation (2) is numerically solved for the mass density using a fourth-order Runge-Kutta algorithm.

2.2 Mass Density Derived from Cutoff Frequencies

The dispersion relationship for a parallel propagating EMIC wave (L mode) in a multi-ion species cold plasma (H^+, He^+, O^+) is (Summers and Thorne, 2003):

$$n^2=1-\frac{\omega_{pe}^2}{\omega\left(\omega+|\Omega_e|\right)}-\sum_{j=1}^{3}\frac{\omega_{pj}^2}{\omega\left(\omega-\Omega_j\right)}, \tag{3}$$

where n is the index of refraction, ω is the wave frequency, ω_{pe} is the electron plasma frequency, Ω_e is the electron gyrofrequency, ω_{pj} is the ion plasma frequency, Ω_j is the ion gyrofrequency, and the suffix j denotes ion species (H^+, He^+, O^+). After some algebra and approximations, the cutoff frequencies, where $n^2 = 0$, as functions of ion concentrations (η_j) are as follows (Min et al., 2015):

$$\omega_{H^+,co}=\frac{\Omega_{H^+}}{32}\left(5+12\eta_{He^+}+15\eta_{O^+}+FF\right), \tag{4}$$

$$\omega_{He^+,co}=\frac{\Omega_{H^+}}{32}\left(5+12\eta_{He^+}+15\eta_{O^+}-FF\right), \tag{5}$$

$$FF=3\sqrt{16\eta_{He^+}^2+\left(1-5\eta_{O^+}\right)^2+8\eta_{He^+}\left(1+5\eta_{O^+}\right)}, \tag{6}$$

$$n_e=n_i\left(\eta_{H^+}+\eta_{He^+}+\eta_{O^+}\right), \tag{7}$$

where η_{H^+}, η_{He^+}, and η_{O^+} are the concentrations of H^+, He^+, and O^+, respectively. $\omega_{H^+,co}$ denotes the H band cutoff frequency, while $\omega_{He^+,co}$ denotes the He band cutoff frequency. Ω_{H^+} is the H^+ gyrofrequency. Equation (7) maintains the electrical neutrality (electron number density n_e equals ion number density n_i). The ion concentrations can easily be obtained by solving the Equations (4), (5), and (7). Then the local mass density ρ_0 is:

$$\rho_0=n_i\left(\eta_{H^+}+4\eta_{He^+}+16\eta_{O^+}\right). \tag{8}$$

The equatorial mass density ρ_{eq} is obtained by bringing back ρ_0 to Equation (1).

3. Observations and Analyses

Toroidal Alfvén waves and EMIC waves were simultaneously observed by the Van Allen Probe-B between 05:30:00 UT and 08:30:00 UT on Aug. 29, 2017. The observations consist of combined data from Electric and Magnetic Field Instrument Suite and Integrated Science (EMFISIS) (Kletzing et al., 2013), Electric Field and Waves Suite (EFW) (Wygant et al., 2013), and Helium, Oxygen, Proton, and Electron (HOPE) mass spectrometer (Funsten et al., 2013) instruments on board the Van Allen Probe-B.

3.1 Two Band EMIC Waves

The electron number density (n_e), EMIC wave power spectral density (PSD), ellipticity (ε), and wave normal angle (θ) are displayed in Figures 1a–1d, respectively. The PSD is obtained by applying Fast Fourier Transform (FFT) to the 64 Hz resolution magnetic fields with a 128 s sliding window and a 43 s moving forward step. The two black solid curves in Figures 1b–1d denote the local He^+ (Ω_{He^+}, upper) and O^+ (Ω_{O^+}, lower) gyrofrequencies, respectively. The waves are observed in post-noon sector (MLT from ~12 hr to ~14 hr) near the magnetic equator (MLAT from −12° to −6°) with L value from ~5.6R_E to ~5.8R_E. Figures 1c and 1d show that the EMIC waves have mixed left-hand and linear polarizations with small normal angles. In order to determine the ion components accurately, we choose data from 07:45:41 UT to 07:50:41 UT corresponding to the time interval (300 s) between two vertical dashed lines in Figures 1b–1d to perform FFT. The time-averaged PSD is used for cutoff frequency determination (results with input spectra from different times are also checked; the resultant average ion mass has a minor change). The corresponding PSD is displayed in Figure 1e. The cutoff frequencies are determined through the following: (1) PSD(f+df)–PSD(f) > 0.5×10^{-3} nT^2/Hz. (2) PSD(f+2×df)–PSD(f) > 1×10^{-3} nT^2/Hz. (3) PSD(f)–PSD(f–df) < 0.5×10^{-3} nT^2/Hz. (4) PSD(f)–PSD(f–2×df) < 1×10^{-3} nT^2/Hz, (5) PSD(f) < 5×10^{-3} nT^2/Hz, where PSD(f) is the wave power spectral density at frequency f, and df is the frequency resolution. Then,

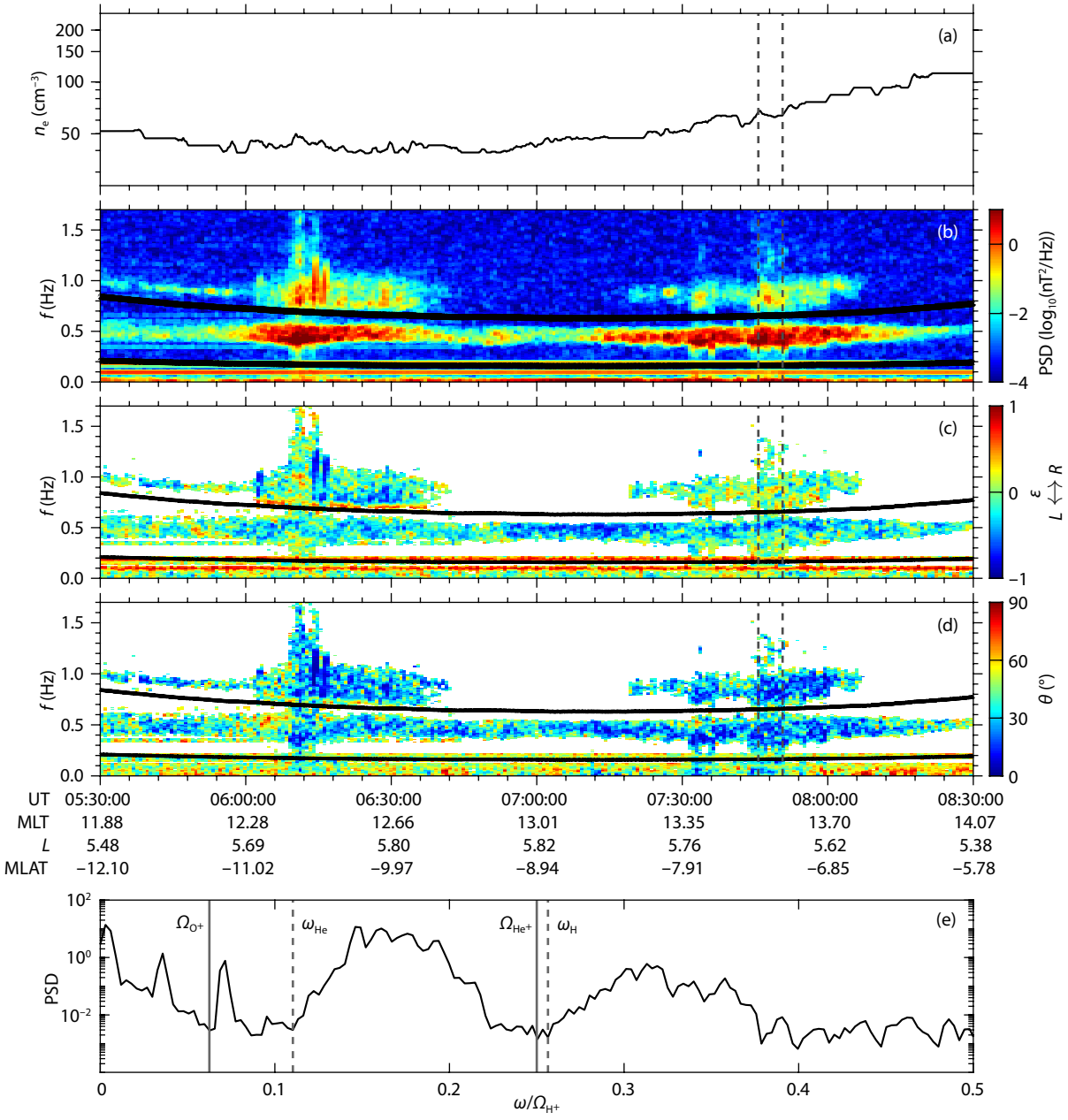

Figure 1. H$^+$ band and He$^+$ band EMIC waves observed by the Van Allen Probe-B on Aug. 29, 2017. (a) Electron density. (b) Wave power spectra. (c) Ellipticity ε. (d) Wave normal angle θ. (e) Averaged wave power spectrum from 07:45:41 UT to 07:50:41 UT (interval between two vertical dashed lines in (a)–(d)). The two black solid curves in (b)–(d) denote the He$^+$ (upper) and O$^+$ (lower) gyrofrequency (Ω_{He^+} and Ω_{O^+}), respectively. In panel (e) the vertical dashed lines denote the estimated cutoff frequencies (ω_H and ω_{He}).

the manually selected cutoff frequencies are $\omega_{He} \sim 0.1103\Omega_{H^+}$ and $\omega_H \sim 0.2564\Omega_{H^+}$ (denoted by two vertical dashed lines in Figure 1e), corresponding to $\eta_{H^+} = 94.09\%$, $\eta_{He^+} = 0.64\%$, and $\eta_{O^+} = 5.27\%$ derived by Equations (4), (5), and (7). The local mass density ρ_0 is estimated as ~116.4 amu/cm^3 with electron number density n_e ~64.3 cm^{-3}. Hence the equatorial mass density is $\rho_{eq} = \rho_0(R/LR_E)^\alpha$, and parameter α is left to be determined by toroidal Alfvén waves.

3.2 Magnetoseismic Analyses

We smooth the 1 Hz resolution magnetic fields with a 90 s sliding window to obtain the background magnetic fields. Then we subtract the background from the magnetic fields to get the magnetic fluctuations. The magnetic fluctuations in GSE coordinates are transformed to magnetic field aligned (MFA) coordinate system with azimuthal component B_ϕ, radial component B_r and compressional component B_z. Only the electric field components E_y and E_z in the MGSE coordinates obtained from the EFW are used here because the component E_x along the spin axis is less accurate. We obtain the three dimensional electric field (E_ϕ, E_r, and E_z) in MFA coordinate system under the assumption of $\boldsymbol{E}\cdot\boldsymbol{B} = 0$. This method works well because the angle between the magnetic field line and the spacecraft spin plane is larger than 15° in this case. The PSD of ULF wave is obtained by applying a 30 min FFT sliding window and a 5 min moving forward step to fields in MFA coordinates.

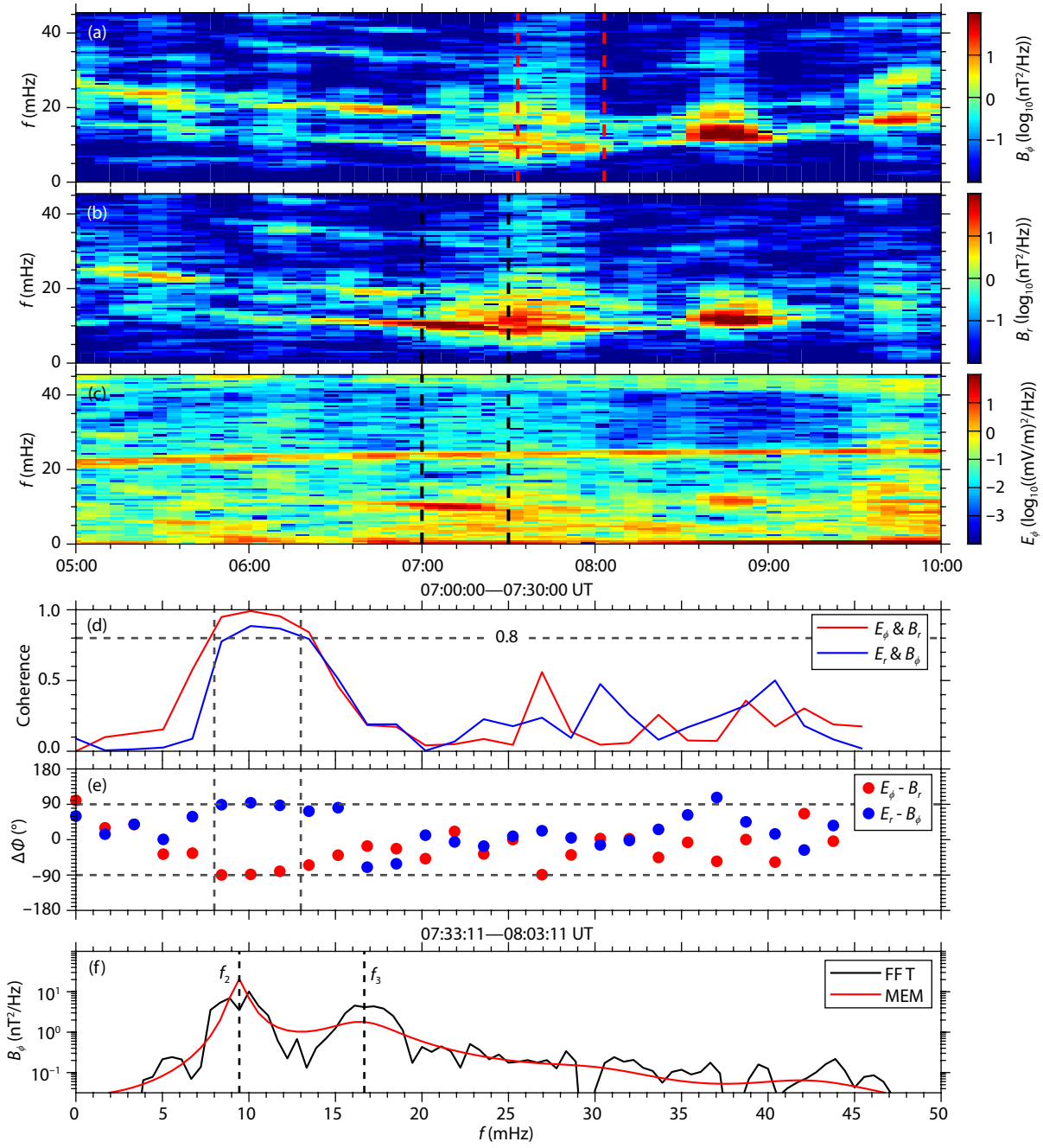

Figure 2. Wave power spectra of (a) B_ϕ, (b) B_r, and (c) E_ϕ. (d) Coherence of E_ϕ & B_r (red line) and E_r & B_ϕ (blue line). (e) Phase difference between E_ϕ & B_r (red dots) and E_r & B_ϕ (blue dots). Coherence and phase difference are derived from fields between 07:00:00 UT and 07:30:00 UT (two black dashed lines in (b) and (c)). (f) Wave power spectrum for fields between 07:33:11 UT and 08:03:11 UT (30 min, between two red dashed lines in (a)) estimated by FFT (black curve) and MEM (red curve).

Figures 2a–2c show the PSD of B_ϕ, B_r, and E_ϕ from 05:00:00 UT to 10:00:00 UT, respectively. In order to determine the harmonic number, we separately select the fields in MFA coordinate system from 07:00:00 UT to 07:30:00 UT (two black dashed lines in Figures 2b and 2c) to check the coherence and phase difference ($\Delta\Phi$) with a 600 s sliding window and 400 s overlap, which are shown in Figures 2d and 2e, respectively. We choose this time interval because there are simultaneously enhanced PSD in (a)–(c) at ~10 mHz. Two vertical black dashed lines in Figures 2d and 2e denote the large coherence (> 0.8) between E_ϕ & B_r and E_r & B_ϕ at ~10 mHz. The corresponding phase difference shows ~ −90° for E_ϕ–B_r (poloidal mode) and ~90° for E_r–B_ϕ (toroidal mode). Because the phase of E_ϕ (E_r) lags (leads) B_r (B_ϕ) by 90° for the poloidal (toroidal) mode even harmonic for the measurements made slightly south of the magnetic equator (Takahashi et al., 2011), the harmonic at ~10 mHz is an even mode. In addition, for the power law density model, the spacing between the successive harmonics, f_{n+1}–f_n, is approximately identical (Schulz, 1996; Takahashi and Denton, 2007), and one more visible harmonic exists below this even mode (see Figure 2a, 05:00 UT to 06:30 UT, ~6 mHz). Hence, the emission at ~10 mHz is considered to be the second harmonic.

We apply FFT to the fields between 07:33:11 UT and 08:03:11 UT (30 min, denoted by two red vertical dashed lines in Figure 2a, the same central time as Figure 1e) when EMIC waves coexisted to determine harmonic frequencies, which is denoted by the black line in Figure 2f. The red solid curve is the estimated PSD using a maximum entropy method (MEM) similar to Takahashi and Denton (2007). We adjust the order of MEM approximation to find the best representative spectral peaks of f_2 and f_3. The harmonic f_2 ~9.44 mHz and f_3 ~16.67 mHz are selected for magnetoseismic analyses due to their stronger power and distinct harmonic structure.

A dipole magnetic field model is adopted because, during the interval, there is small difference of the field line calculated by the dipole model and the TS05 model (Tsyganenko and Sitnov, 2005), and the magnetic field derived from the dipole model (~170 nT) is close to the observation (~172 nT). Assuming the field line is fixed at an altitude of 100 km, we numerically solve Equation (2) for theoretical harmonic frequencies with ρ_{eq} determined in Section 3.1 through altering α from −6 to 6. The best parameter α_{best} is determined from the best fit between theoretical and observed frequencies ($f_{n,th}$ and $f_{n,obs}$) by minimizing the quantity,

$$S = \sqrt{\frac{1}{N}\sum\left(\frac{f_{n,obs} - f_{n,th}}{f_{n,obs}}\right)^2}, \tag{9}$$

where N is the number of harmonics used and subscript n is harmonic labels. For a spectrum with resolution of 0.56 mHz (signal length of 30 min), the error in manually harmonic determination is ~0.05. We find $\alpha = -5.0 \sim -2.9$ ($S < 0.05$) with $\alpha_{best} = -3.8$ (minimum $S < 0.04$). The negative α indicates that the mass density reaches a local peak at the equator and reduces toward larger latitudes. To note, in a real sense the mass density will finally increase with latitude as the magnetic field line approaches the ionosphere. The value of $\alpha < 0$ exists because the magnetic field line near the equator plays a main role in the Alfvén frequency determination (Denton et al., 2006). Based on the WKB formula for the Alfvén frequency $1/f \approx \int \mathrm{d}s/V_A$, at higher latitudes the magnetic field is stronger and hence V_A is larger, placing less effect on the values of the frequencies.

For a dipole magnetic field with a power law distribution, the separation between the successive harmonics does not depend significantly on the harmonic number (Schulz, 1996; Takahashi and Denton, 2007). The relationship between the parameter α and the harmonic frequency separation is introduced by Takahashi and Denton (2007). The normalized frequency separation $\bar{f} = (f_{n+1} - f_n)/f_3$ decreases from ~0.40 for $\alpha = -6$ to ~0.33 for $\alpha = 6$, while for $\alpha = 0$ the separation is ~0.38. Hence, a smaller α corresponds to a broader normalized frequency separation. We apply a 30 min sliding FFT window and a 15 min advancing step to B_ϕ to determine the harmonic frequency for frequency separation checking. For every spectral line, peaks with spectral width at 75% of the peak intensity (> 0.1 nT^2/Hz) less than 3 mHz are selected. Then, we eliminate the outliers and manually choose the most representative frequencies. Figure 3a shows the PSD of B_ϕ with harmonic frequencies (black dots) over-plotted. EMIC wave amplitudes are shown in Figure 3b (H band and He band are denoted by red and blue lines, respectively). The normalized frequency separations $\bar{f}$ with error bars are shown in Figure 3c. Obviously, $\bar{f}$ is larger (~0.4–~0.45) when EMIC waves show up (between two red dashed lines), corresponding to smaller α (< 0) than most of those outside of this time interval ($\bar{f} < 0.38$ and $\alpha > 0$). This agrees with the result of the theoretical calculation (Takahashi and Denton, 2007). The presence of EMIC waves and broader harmonic frequencies indicates that the equatorial mass density peaks are possibly triggered by EMIC waves.

3.3 Ion Measurements

We divide the case into Event 1 (time before 07:00:00 UT) and Event 2 (time after 07:00:00 UT) according to the EMIC waves' intensities. Figures 4a and 4b show the electron number densities (n_e) derived from upper hybrid frequencies of Event 1 (left) and Event 2 (right), respectively. Figures 4c and 4d show the ion number densities for H^+ (n_H, red lines), He^+ (n_{He}, magenta lines), O^+ (n_O, cyan lines), and ensemble ($n_{total} = n_H + n_{He} + n_O$, black lines) obtained from HOPE flux data with energies < 100 eV. Figures 4e and 4f show the mass density ($\rho = n_H + 4n_{He} + 16n_O$, blue dots) and average ion mass ($M = \rho/n_{total}$, red dots) with densities obtained from Figures 4c and 4d. There are ions with low energy undetected by the HOPE instruments, hence the electron number density and ion number density are different as shown in Figures 4a–4d. Solid curves denote 15-point smoothed values. H band (red lines) and He band (blue lines) EMIC wave amplitudes are shown in Figures 4g and 4h. Low energy H^+, He^+, and O^+ fluxes are displayed in Figures 4 (i, k, m) and (j, l, n), respectively. All fluxes are summed over the energy interval titled above each panel. The proportion of higher energy (> 100 eV) ion fluxes are very small, hence they are not included. As EMIC waves show up, H^+ fluxes are significantly enhanced and become more concentrated near pitch angle at 90° (Figures 4c and 4h), which indicates a trapping distribution of these low energy H^+. He^+ fluxes show a weaker relation with the waves in Figures 4k and 4l, and weaker anisotropic distribution is found. No simultaneously enhanced flux of O^+ is observed, as shown in Figures 4m and 4n. Hence, as in Figures 4c and 4d, n_H, n_{He}, and n_{total} increase with enhanced wave amplitudes, while n_O remains small and almost constant. In addition, the simultaneous increases of n_e and n_{total} are well-correlated with wave emissions and trapping H^+ fluxes, indicating certain modulation mechanisms among them. The coexistence of enhanced wave amplitudes and trapped H^+ fluxes indicate that low energy H^+ ions should be perpendicularly heated by the EMIC waves. Heating of low energy ions by EMIC waves has been observed and simulated by many previous researchers (Gary et al., 1995; Omidi et al., 2010; Bortnik et al., 2010; Kitamura et al., 2018; Yu XD and Yuan ZG, 2019). Cold protons have a non-resonant interaction with enhanced proton-cyclotron-like fluctuations generated near the magnetic equator (Gary et al., 1995). The non-resonant character of this interaction has been confirmed by Anderson and Fuselier (1994), and their observations show that the low-energy protons' perpendicular temperature increase is always observed at 90° pitch angles. The simulation results of Yu XD and Yuan ZG (2019) also show that, under the influence of the EMIC wave, the perpendicular beta (temperature) of the cold protons increases significantly, while the parallel beta (temperature) remains almost unchanged. Thus, the perpendicular heating of the cold protons can

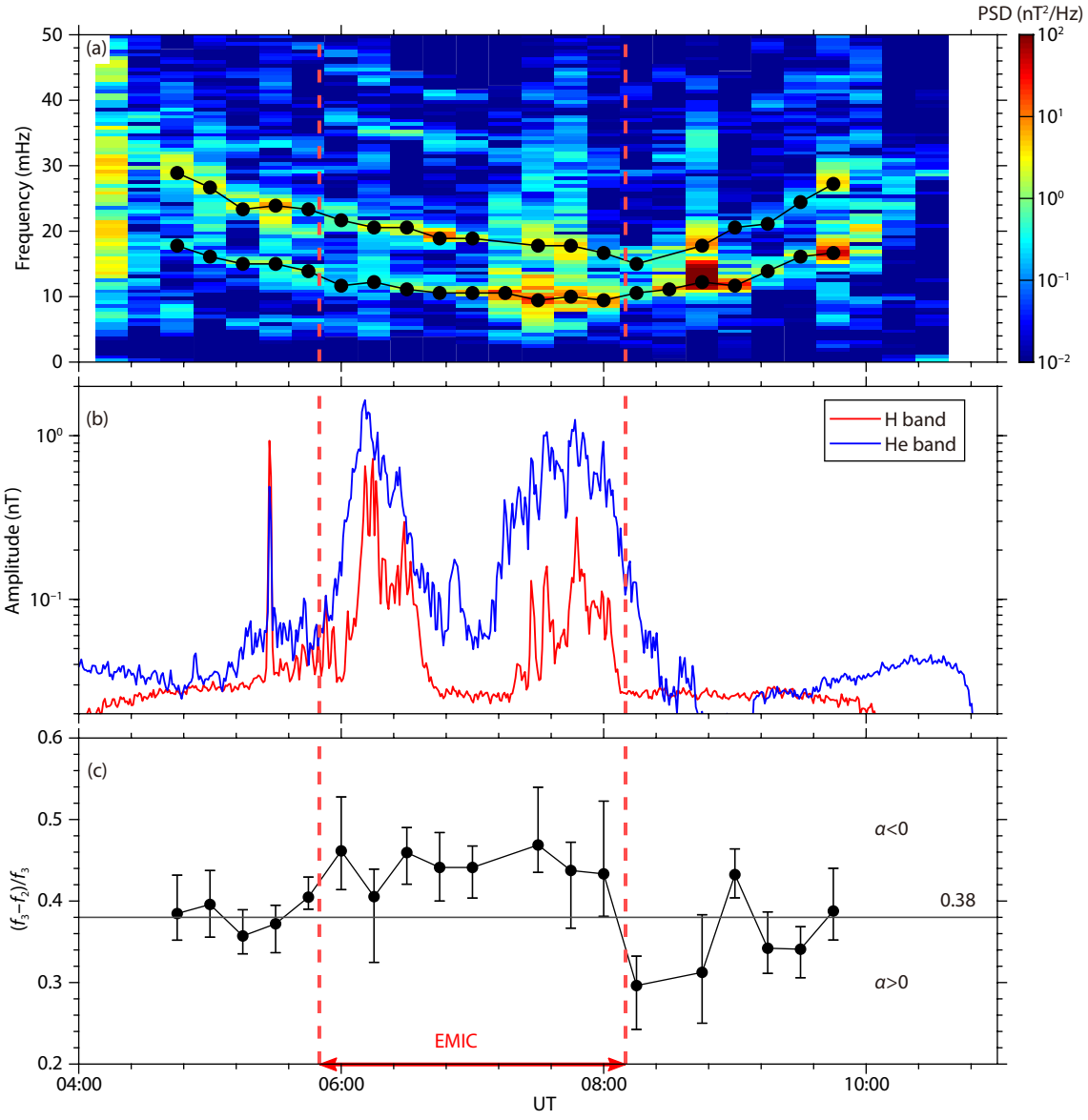

Figure 3. (a) Wave power spectra of ULF waves with harmonic frequencies denoted by black dots. (b) Amplitudes for H^+ band (red line) and He^+ band (blue line) EMIC waves. (c) $(f_3-f_2)/f_3$ denoted by black dots. Red vertical dashed lines denote the existence of EMIC emission.

be explained by the non-resonance interaction with the EMIC waves. Ions with larger equatorial pitch angles will mirror at lower latitudes and may lead to higher ion abundances near the equator. Therefore, by investigating the measured ion fluxes, we find that the peak formation is most likely due to the enhanced ion abundances at equator, which are triggered by EMIC waves' perpendicular heating on low energy ions. Figures 4e and 4f illustrate that ρ (black lines) increases while M (red lines) decreases when EMC waves exist. Since ρ is the product of M and number density n, the formation of a local mass density peak can be attributed to a dominant increase of n at the equator.

4. Discussion

According to Liouville's theorem, for a bi-Maxwellian distribution with $A > 1$ ($A < 1$) the integral number density will decrease (increase) towards higher latitudes along the field line, while for $A = 1$ the number density will be constant (Roederer and Zhang H, 2014). A is the temperature anisotropy (perpendicular temperature divided by parallel temperature). For quantitative analyses, we convert the time averaged H^+ fluxes to phase space densities in two time intervals as denoted by two black vertical lines in Figure 4c (06:08:24 UT to 06:13:24 UT of Event 1) and Figure 4h (07:44:12 UT to 07:47:12 UT of Event 2), respectively. Then, we adopt the bi-Maxwellian distribution to fit the ion phase space densities (Yuan ZG et al., 2019) with energy < ~100 eV and map the number densities along the field line according to Liouville's theorem. Unfortunately, the measured O^+ fluxes are too deficient to perform fitting (as shown in Figures 4m and 4n). Because no directional preference is observed in low energy O^+ fluxes, we assume the observed O^+ distribution has $A = 1$, $n_{O+} = 0.0649$ cm^{-3} of Event 1 and $A = 1$, $n_{O+} = 0.0388$ cm^{-3} of Event 2 (densities are derived from HOPE by adding all fluxes with energy level < 100 eV). The fitting parameters for H^+, He^+, and O^+ are displayed in Table 1.

Liouville's theorem states that the distribution function $f(\boldsymbol{r}, \boldsymbol{v}, t)$

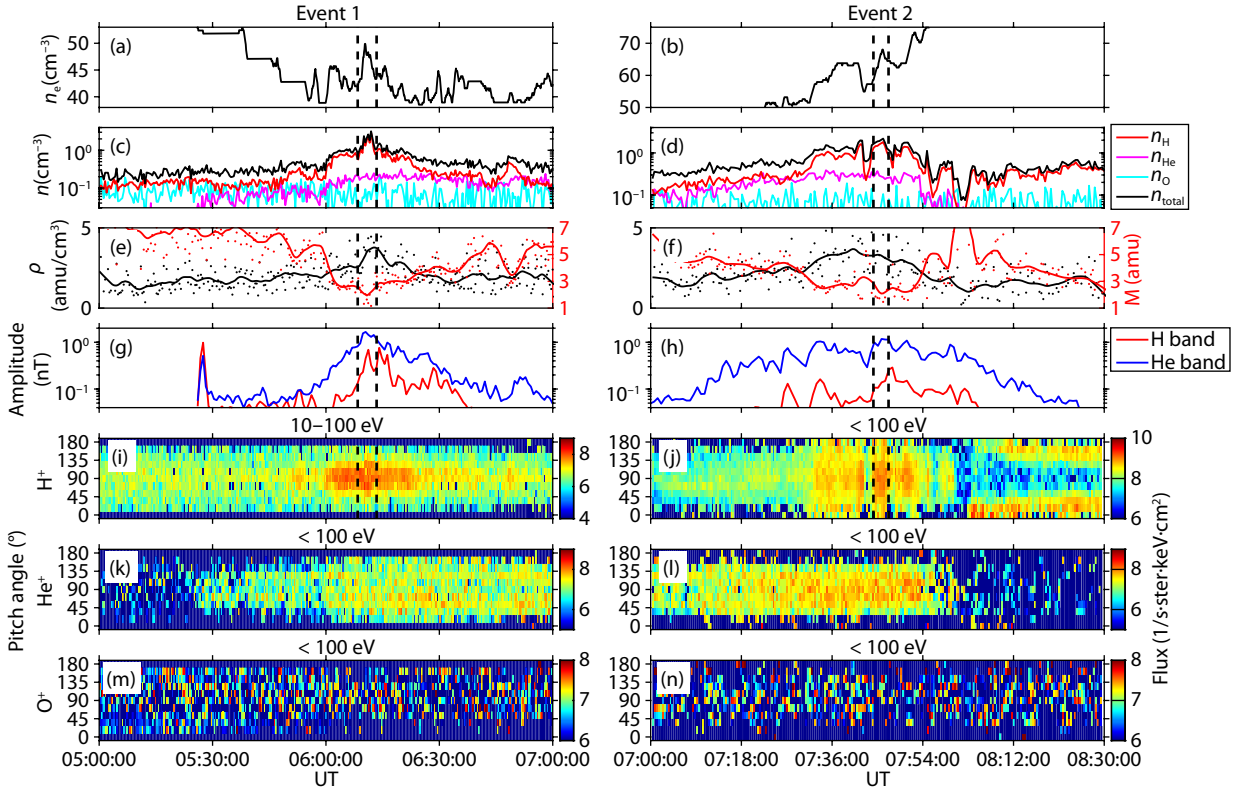

Figure 4. (a) (b) Electron number densities derived from upper hybrid frequencies. (c) (d) Ion number densities for H^+ (n_H, red lines), He^+ (n_{He}, magenta lines), O^+ (n_O, cyan lines), and ensemble ($n_{total} = n_H + n_{He} + n_O$, black lines) obtained from HOPE fluxes data with energy < 100 eV. (e) (f) Mass density ($\rho = n_H + 4n_{He} + 16n_O$, blue dots) and average ion mass ($M = \rho/n_{total}$, red dots). Solid curves denote 15-point smoothed values. (g) (h) EMIC wave amplitudes. (i) (j), (k) (l), and (m) (n) show the pitch angle distributions of fluxes of H^+, He^+, and O^+, respectively. All fluxes are averaged over the energy interval titled above each panel.

along a single particle trajectory through any point ($\boldsymbol{r}$(t), $\boldsymbol{v}$(t)) in phase space is constant, which means that $f(\boldsymbol{r}(t), \boldsymbol{v}(t), t) = f(\boldsymbol{r}_0, \boldsymbol{v}_0, 0)$ with initial condition $\boldsymbol{r}(0) = \boldsymbol{r}_0$ and $\boldsymbol{v}(0) = \boldsymbol{v}_0$. For simplicity, we assume fitted ions are trapped on dipole field lines under adiabatic conditions. We still uphold some basic restrictions, i.e. absence of field-aligned electric fields, no time-variations, and symmetric angular distributions everywhere (Roederer and Zhang H, 2014). We choose the distribution function $f(T_0, \mu_0)$ at the magnetic equator and $f(T_s, \mu_s)$ at point s on the same field line, where $T = mv^2/2$, m is the particle rest mass, v is the particle velocity, μ is the cosine value of the pitch angle α. This gives us:

$$n_s = n_0 \frac{2B_s}{B_0} \int_0^{\infty} \int_{\mu_0^*}^{1} f(T_0, \mu_0) \frac{\mu_0 \mathrm{d}\mu_0 \mathrm{d}T_0}{\sqrt{1 - \left(\frac{B_s}{B_0}\right)\left(1 - \mu_0^2\right)}}, \tag{10}$$

$$f(T_0, \mu_0) = \frac{1}{A} \sqrt{\frac{T_0}{\pi T_{\parallel}^3}} \cdot \mathrm{e}^{-\frac{T_0}{AT_{\parallel}}\left(1 + A\mu_0^2 - \mu_0^2\right)}, \tag{11}$$

where n_s and n_0 are the number densities at point s and the equator, respectively. B_s and B_0 are the corresponding magnetic fields at two points (dipole model is used here). Particles with μ below the limiting value $\mu_0^* = (1 - B_0/B_s)^{0.5}$ at the equator will mirror before reaching point s. The integral of $f(T_0, \mu_0)$ over $0 < T_0 < \infty$ and $-1 < \mu_0 < 1$ is equal to 1. The fitted parameters in Table 1 are considered as the equatorial ion distribution parameters since the observations are made close to the magnetic equator. Figures 5a and 5b show the field line mass density distributions of H^+(ρ_H, red curve), He^+(ρ_{He}, magenta curve), O^+(ρ_O, cyan curve), and ensemble (ρ_{total}, black curve) of Event 1 (left column) and Event 2 (right column), respectively. The total mass density can be expressed as $\rho_{total} = n_H + 4n_{He} + 16n_O = \rho_H + \rho_{He} + \rho_O$. Figures 5c and 5d display the distributions of mass densities normalized to their equatorial values. Evidently, the total mass density in each event has a local peak at equator, which is consistent with the prediction of our wave frequency analyses. Power law distributions with $\alpha = -5.0$ (black dotted dashed curve), -3.8 (green solid curve), and -2.9 (black dashed curve) obtained from Section 3 are also displayed in Figure 5d for comparison. These illustrate that, though the ions measured by the HOPE occupy only a small part of the ensemble due to the limitation of *in situ* detection, the distribution of ρ_{total} is approximately in line with the power law distribution derived from frequency analyses. Additionally, the electron number densities derived from upper hybrid frequencies increase together with enhanced H^+ fluxes, which is denoted by two dashed vertical lines in Figures 4a, 4c, 4f, and 4h, respectively. The electron number densities have increases of 6–10 cm^{-3}, corresponding to an enhancement of 10%–25% from the ambient electron densities. Under the assumption of quasi-neutrality of plasma, the obvious enhancements of electron densities also support equatorial ion concentrations under the influence of EMIC waves. The observed mass density peaks are located in the post-noon sector with MLT ~13 hr where a negative α is possible to ap-

Table 1. Fitting parameters for H^+, He^+, and O^+ obtained from HOPE flux data with energy < ~100 eV.

			n/cm^{-3}	$T_{\|\|}$/eV	A
H^+	Event 1	1	1.253	1.1745	2.1511
		2	0.2606	1.6912	0.3086
		3	0.3831	4.6979	1.960
		4	0.0601	42.2808	1.2346
	Event 2	1	2.0794	1.6735	1.2142
		2	0.2412	13.0496	0.5776
He^+	Event 1	1	0.5031	1.4383	0.7525
		2	0.1809	4.6979	1.6044
		3	0.2003	28.5839	1.4792
	Event 2	1	0.5196	1.0825	1.5625
		2	0.3004	9.2078	1.5329
		3	0.0653	63.1601	1.7617
O^+	Event 1	1	0.0649	–	1
	Event 2	1	0.0388	–	1

Note: Bi-Maxwellian distribution: $f(v_{||}, v_\perp) = \frac{1}{\pi^{3/2} V_{||} V_\perp^2} e^{-\frac{v_{||}^2}{V_{||}^2}} e^{-\frac{v_\perp^2}{V_\perp^2}}$, $T_{||,\perp} = \frac{1}{2} m V_{||,\perp}^2$, $A = \frac{T_\perp}{T_{||}}$.

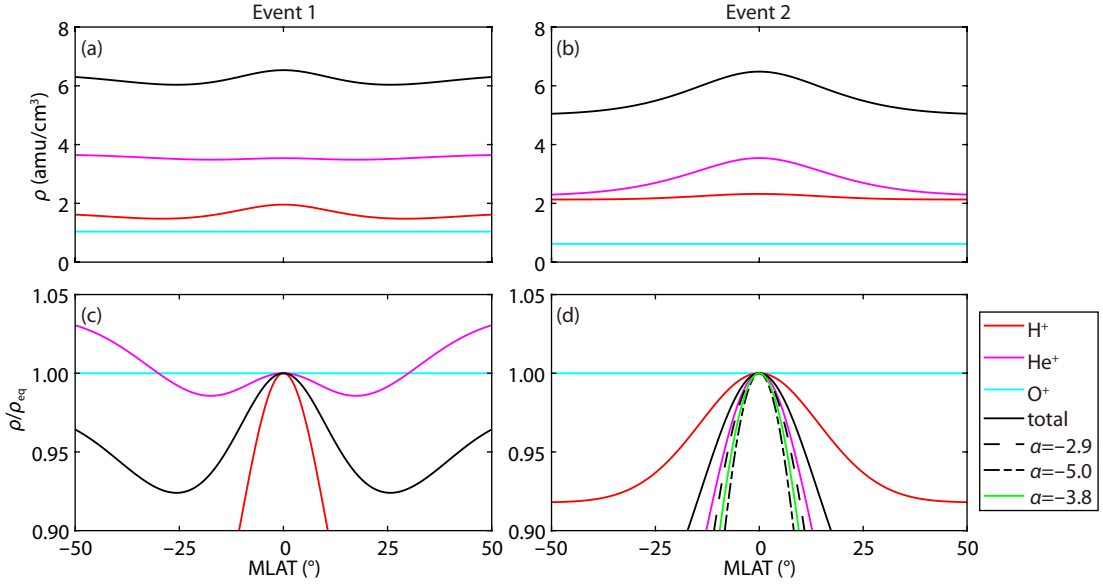

Figure 5. (a) (b) H^+ (red curve), He^+ (magenta curve), O^+ (cyan curve), and total (black curve) mass density distributions with respect to the MLAT of Event 1 (left) and Event 2 (right). (c) (d) Mass density distributions normalized to their equatorial values. Power law distributions with $\alpha = -5.0$ (black dotted dashed curve), −3.8 (green solid curve), and −2.9 (black dashed curve) are also displayed in (d) for comparison.

pear (Denton et al., 2004, 2006, 2015; Takahashi and Denton, 2007). If the peaks in Figure 2f are also taken to be the fourth and fifth (or sixth) harmonics, α will be larger than 6, which is unrealistic and, to our knowledge, nobody has reported values of $\alpha > 6$.

5. Summary

Through frequency analyses of simultaneously observed toroidal harmonics and EMIC waves, equatorial mass density peaks are determined. The distributions of measured low energy ions support the mass density peak formation at the equator according to Liouville's theorem. An increase of perpendicular fluxes of ions (< 100 eV) heated by EMIC waves can promote mass density peak formation at the equator. This paper thus provides observational evidence that equatorial mass density peaks are formed due to equatorial ion concentrations triggered by EMIC waves. In turn, equatorial mass density peaks influence the excitation and propagation of magnetohydrodynamic waves, which will be investigated in future work.

Acknowledgments

We acknowledge the Van Allen Probes data from the EMFISIS, EFW, and HOPE instruments obtained from http://emfisis.physics.uiowa.edu/Flight/RBSP-B/, http://rbsp.space.umn.edu/data/rbsp/rbspb/l3/, https://rbsp-ect.lanl.gov/data_pub/rbspb/hope/level3/, respectively. This work is supported by the National Natural Science Foundation of China (41925018, 41874194).

References

Anderson, B. J., &Fuselier, S. A. (1994). Response of thermal ions to electromagnetic ion cyclotron waves. *Journal of Geophysical Research*, *99*(A10), 19,413–19,425. https://doi.org/10.1029/94JA01235

André, M., and Cully, C. M. (2012). Low-energy ions: a previously hidden solar system particle population. *Geophys. Res. Lett.*, *39*(3), L03101. https://doi.org/10.1029/2011GL050242

Angerami, J. J., and Thomas, J. O. (1964). Studies of planetary atmospheres: 1. The distribution of electrons and ions in the Earth's exosphere. *J. Geophys. Res.*, *69*(21), 4537–4560. https://doi.org/10.1029/JZ069i021p04537

Bortnik, J., Thorne, R. M., and Omidi, N. (2010). Nonlinear evolution of EMIC waves in a uniform magnetic field: 2. Test-particle scattering. *J. Geophys. Res. Space Phys.*, *115*(A12), A12242. https://doi.org/10.1029/2010JA015603

Denton, R. E., Takahashi, K., Anderson, R. R., and Wuest, M. P. (2004). Magnetospheric toroidal Alfvén wave harmonics and the field line distribution of mass density. *J. Geophys. Res. Space Phys.*, *109*(A6), A06202. https://doi.org/10.1029/2003JA010201

Denton, R. E. (2006). Magneto-seismology using spacecraft observations. In K. Takahashi, et al. (Eds.), Magnetospheric ULF Waves: Synthesis and New Directions. American Geophysical Union. https://doi.org/10.1029/169GM20

Denton, R. E., Takahashi, K., Galkin, I. A., Nsumei, P. A., Huang, X., Reinisch, B. W., Anderson, R. R., Sleeper, M. K., and Hughes, W. J. (2006). Distribution of density along magnetospheric field lines. *J. Geophys. Res. Space Phys.*, *111*(A4), A04213. https://doi.org/10.1029/2005JA011414

Denton, R. E., Takahashi, K., Lee, J., Zeitler, C. K., Wimer, N. T., Litscher, L. E., Singer, H. J., and Min, K. (2015). Field line distribution of mass density at geostationary orbit. *J. Geophys. Res. Space Phys.*, *120*(6), 4409–4422. https://doi.org/10.1002/2014JA020810

Eviatar, A., Lenchek, A. M., and Singer, S. F. (1964). Distribution of density in an ion-exosphere of a nonrotating planet. *Phys. Fluids*, *7*(11), 1775–1779. https://doi.org/10.1063/1.2746776

Funsten, H. O., Skoug, R. M., Guthrie, A. A., MacDonald, E. A., Baldonado, J. R., Harper, R. W., Henderson K. C., Kihara K. H., Lake J. E., … Chen, J. (2013). Helium, Oxygen, Proton, and Electron (HOPE) mass spectrometer for the Radiation Belt Storm Probes mission. *Space Sci. Rev.*, *179*(1-4), 423–484. https://doi.org/10.1007/s11214-013-9968-7

Gary, S. P., Thomsen, M. F., Yin, L., and Winske, D. (1995). Electromagnetic proton cyclotron instability: interactions with magnetospheric protons. *J. Geophys. Res. Space Phys.*, *100*(A11), 21961–21972. https://doi.org/10.1029/95JA01403

Huang, Z., Yuan, Z. G., and Yu, X. D. (2020). Evolutions of equatorial ring current ions during a magnetic storm. *Earth Planet. Phys.*, *4*(2), 131–137. https://doi.org/10.26464/epp2020019

Kim, E. H., Johnson, J. R., Kim, H., and Lee, D. H. (2015). Inferring magnetospheric heavy ion density using EMIC waves. *J. Geophys. Res. Space Phys.*, *120*(8), 6464–6473. https://doi.org/10.1002/2015JA021092

Kitamura, N., Kitahara, M., Shoji, M., Miyoshi, Y., Hasegawa, H., Nakamura, S., Katoh, Y., Saito, Y., Yokota, S., … Burch, J. L. (2018). Direct measurements of two-way wave-particle energy transfer in a collisionless space plasma. *Science*, *361*(6406), 1000–1003. https://doi.org/10.1126/science.aap8730

Kletzing, C. A., Kurth W. S., Acuna M., MacDowall R. J., Torbert R. B., Averkamp T., Bodet D., Bounds S. R., Chutter M., … Tyler J. (2013). The Electric and Magnetic Field Instrument Suite and Integrated Science (EMFISIS) on RBSP. *Space Sci. Rev.*, *179*(1-4), 127–181. https://doi.org/10.1007/s11214-013-9993-6

Meredith, N. P., Thorne, R. M., Horne, R. B., Summers, D., Fraser, B. J., and Anderson, R. R. (2003). Statistical analysis of relativistic electron energies for cyclotron resonance with EMIC waves observed on CRRES. *J. Geophys. Res. Space Phys.*, *108*(A6), 1250. https://doi.org/10.1029/2002JA009700

Lemaire, J. F., and Gringauz, K. I. (1998). The Earth's Plasmasphere. New York: Cambridge University Press.

Min, K., Bortnik, J., Denton, R. E., Takahashi, K., Lee, J. and Singer, H. J. (2013). Quiet time equatorial mass density distribution derived from AMPTE/CCE and GOES using the magnetoseismology technique. *J. Geophys. Res. Space Phys.*, *118*(10), 6090–6105. https://doi.org/10.1002/jgra.50563

Min, K., Liu, K. J., Bonnell, J. W., Breneman, A. W., Denton, R. E., Funsten, H. O., Jahn, J. M., Kletzing, C. A., Kurth, W. S., Larsen, B. A., Reeves, G. D., Spence, H. E., and Wygant, J. R. (2015). Study of EMIC wave excitation using direct ion measurements. *J. Geophys. Res. Space Phys.*, *120*(4), 2702–2719. https://doi.org/10.1002/2014JA020717

Nosé, M., Oimatsu, S., Keika, K., Kletzing, C. A., Kurth, W. S., De Pascuale, S., Smith, C. W., MacDowall, R. J., Nakano, S., Reeves, G. D., Spence, H. E., and Larsen, B. A. (2015). Formation of the oxygen torus in the inner magnetosphere: Van Allen Probes observations. *J. Geophys. Res. Space Phys.*, *120*(2), 1182–1196. https://doi.org/10.1002/2014JA020593

Omidi, N., Thorne, R. M., and Bortnik, J. (2010). Nonlinear evolution of EMIC waves in a uniform magnetic field: 1. Hybrid simulations. *J. Geophys. Res. Space Phys.*, *115*(A12), A12241. https://doi.org/10.1029/2010JA015607

Press, W. H., Teukolsky, S. A., Vetterling, W. T., and Flannery, B. P. (1997). Numerical Recipes in Fortran 77: The Art of Scientific Computing (Vol. 1 of Fortran Numerical Recipes), 994 pp., New York: The Press Syndicate of the University of Cambridge.

Rauch, J. L., and Roux, A. (1982). Ray tracing of ULF waves in a multicomponent magnetospheric plasma: consequences for the generation mechanism of ion cyclotron waves. *J. Geophys. Res. Space Phys.*, *87*(A10), 8191–8198. https://doi.org/10.1029/JA087iA10p08191

Roederer, J. G., and Zhang, H. (2014). Dynamics of Magnetically Trapped Particles: Foundations of the Physics of Radiation Belts and Space Plasmas. Berlin: Springer. https://doi.org/10.1007/978-3-642-41530-2

Schulz, M. (1996). Eigenfrequencies of geomagnetic field lines and implications for plasma-density modeling. *J. Geophys. Res. Space Phys.*, *101*(A8), 17385–17397. https://doi.org/10.1029/95JA03727

Shi, Q. Q., Hartinger, M., Angelopoulos, V., Zong, Q. G., Zhou, X. Z., Zhou, X. Y., Kellerman, A., Tian, A. M., Weygand J., … Yao, Z. H. (2013). THEMIS observations of ULF wave excitation in the nightside plasma sheet during sudden impulse events. *J. Geophys. Res. Space Phys.*, *118*(1), 284–298. https://doi.org/10.1029/2012JA017984

Singer, H. J., Southwood, D. J., Walker, R. J., and Kivelson, M. G. (1981). Alfven wave resonances in a realistic magnetospheric magnetic field geometry. *J. Geophys. Res. Space Phys.*, *86*(A6), 4589–4596. https://doi.org/10.1029/JA086iA06p04589

Summers, D., and Thorne, R. M. (2003). Relativistic electron pitch-angle scattering by electromagnetic ion cyclotron waves during geomagnetic storms. *J. Geophys. Res. Space Phys.*, *108*(A4), 1143. https://doi.org/10.1029/2002JA009489

Takahashi, K., Denton, R. E., Anderson, R. R., and Hughes, W. J. (2006). Mass density inferred from toroidal wave frequencies and its comparison to electron density. *J. Geophys. Res. Space Phys.*, *111*(A1), A01201. https://doi.org/10.1029/2005JA011286

Takahashi, K., and Denton, R. E. (2007). Magnetospheric seismology using multiharmonic toroidal waves observed at geosynchronous orbit. *J. Geophys. Res. Space Phys.*, *112*(A5), A05204. https://doi.org/10.1029/2006JA011709

Takahashi, K., Glassmeier, K. H., Angelopoulos, V., Bonnell, J., Nishimura, Y., Singer, H. J., and Russell, C. T. (2011). Multisatellite observations of a giant pulsation event. *J. Geophys. Res. Space Phys.*, *116*(11), A11223. https://doi.org/10.1029/2011JA016955

Tsyganenko, N. A., and Sitnov, M. I. (2005). Modeling the dynamics of the inner magnetosphere during strong geomagnetic storms. *J. Geophys. Res. Space Phys.*, *110*(A3), A03208. https://doi.org/10.1029/2004JA010798

Wygant, J. R., Bonnell, J. W., Goetz, K., Ergun, R. E., Mozer, F. S., Bale, S. D., Ludlam, M., Turin, P., Harvey, P. R., … Tao, J. B. (2013). The electric field and waves instruments on the radiation belt storm probes mission. *Space Sci. Rev.*, *179*(1-4), 183–220. https://doi.org/10.1007/s11214-013-0013-7

Yu, X. D., and Yuan, Z. G. (2019). Saturation characteristics of parallel EMIC waves in the inner magnetosphere. *Geophys. Res. Lett.*, *46*(14), 7902–7910. https://doi.org/10.1029/2019GL083630

Yuan, Z. G., Yu, X. D., Ouyang, Z. H., Yao, F., Huang, S. Y., and Funsten, H. O. (2019). Simultaneous trapping of electromagnetic ion cyclotron and magnetosonic waves by background plasmas. *J. Geophys. Res. Space Phys.*, *124*(3), 1635–1643. https://doi.org/10.1029/2018JA026149

Zong, Q. G., Rankin, R., and Zhou, X. Z. (2017). The interaction of ultra-low-frequency Pc3-5 waves with charged particles in Earth's magnetosphere. *Rev. Mod. Plasma Phys.*, *1*, 10. https://doi.org/10.1007/s41614-017-0011-4